Eur J Nucl Med Mol Imaging (2011) 38:1691–1701
DOI 10.1007/s00259-011-1842-9

ORIGINAL ARTICLES

Value of a Dixon-based MR/PET attenuation correction sequence for the localization and evaluation of PET-positive lesions

Matthias Eiber · Axel Martinez-Möller · Michael Souvatzoglou · Konstantin Holzapfel · Anja Pickhard · Dennys Löffelbein · Ivan Santi · Ernst J. Rummeny · Sibylle Ziegler · Markus Schwaiger · Stephan G. Nekolla · Ambros J. Beer

Received: 17 February 2011 / Accepted: 2 May 2011 / Published online: 18 June 2011

Abstract
Purpose In this study, the potential contribution of Dixon-based MR imaging with a rapid low-resolution breath-hold sequence, which is a technique used for MR-based attenuation correction (AC) for MR/positron emission tomography (PET), was evaluated for anatomical correlation of PET-positive lesions on a 3T clinical scanner compared to low-dose CT. This technique is also used in a recently installed fully integrated whole-body MR/PET system.
Methods Thirty-five patients routinely scheduled for oncological staging underwent ^{18}F-fluorodeoxyglucose (FDG) PET/CT and a 2-point Dixon 3-D volumetric interpolated breath-hold examination (VIBE) T1-weighted MR sequence on the same day. Two PET data sets reconstructed using attenuation maps from low-dose CT (PET_{AC_CT}) or simulated MR-based segmentation (PET_{AC_MR}) were evaluated for focal PET-positive lesions. The certainty for the correlation with anatomical structures was judged in the low-dose CT and Dixon-based MRI on a 4-point scale (0–3). In addition, the standardized uptake values (SUVs) for PET_{AC_CT} and PET_{AC_MR} were compared.
Results Statistically, no significant difference could be found concerning anatomical localization for all 81 PET-positive lesions in low-dose CT compared to Dixon-based MR (mean 2.51±0.85 and 2.37±0.87, respectively; p=0.1909). CT tended to be superior for small lymph nodes, bone metastases and pulmonary nodules, while Dixon-based MR proved advantageous for soft tissue pathologies like head/neck tumours and liver metastases. For the PET_{AC_CT}- and PET_{AC_MR}-based SUVs (mean 6.36±4.47 and 6.31±4.52, respectively) a nearly complete concordance with a highly significant correlation was found (r=0.9975, p<0.0001).
Conclusion Dixon-based MR imaging for MR AC allows for anatomical allocation of PET-positive lesions similar to low-dose CT in conventional PET/CT. Thus, this approach appears to be useful for future MR/PET for body regions not fully covered by diagnostic MRI due to potential time constraints.

Matthias Eiber and Axel Martinez-Möller contributed equally.

Stephan G. Nekolla and Ambros J. Beer share joint senior authorship.

M. Eiber (✉) · K. Holzapfel · E. J. Rummeny
Department of Radiology, Klinikum rechts der Isar,
Technische Universität München,
Ismaninger Str. 22,
81675 Munich, Germany
e-mail: matthias.eiber@tum.de

A. Martinez-Möller · M. Souvatzoglou · S. Ziegler · M. Schwaiger · S. G. Nekolla · A. J. Beer
Department of Nuclear Medicine,
Technische Universität München,
Munich, Germany

A. Pickhard
Department of Otorhinolaryngology,
Technische Universität München,
Munich, Germany

D. Löffelbein
Department of Maxillofacial Surgery,
Technische Universität München,
Munich, Germany

I. Santi
Service of Nuclear Medicine, PET Center,
Policlinico S.Orsola-Malpighi, University of Bologna,
Bologna, Italy

Keywords Attenuation correction · Dixon-based VIBE T1-weighted MR sequence · Localization · Low-dose CT · MR/PET

Introduction

The advent of the first integrated MR/positron emission tomography (PET) scanners goes along with huge expectations of a new powerful multimodality imaging tool [1–3]. The reasons for this are based on the advantages MR offers in comparison to CT: an improved soft tissue contrast for e.g. bone marrow lesions, soft tissue tumours and the liver, the possibility of performing functional MR imaging like diffusion, perfusion and MR spectroscopy, and finally the lack of radiation exposure [4–12].

Integrated PET/CT systems use the X-ray source to create an aligned CT data set and transform the CT HU to attenuation factors at 511 keV [13]. However, as the MR signal is not directly related to the radiodensity, conventional MR data cannot be used for attenuation correction (AC) [14]. Thus, as new approaches for a MR/PET system are needed, recently different methods for whole-body MR-based AC of PET data were presented.

Initial trials with an anatomically based attenuation map proved to be unsatisfactory due to interpatient variability [14]. For neurological imaging, trials with an ultrashort echo time technique to distinguish air and cortical bone have been proposed [15–17], as well as approaches consisting in automatic pattern recognition in combination with an atlas [18, 19]. For whole-body imaging, the methods proposed rely on automatic segmentation of different tissue types [20–22]. Martinez-Möller et al. reported a technique involving the segmentation of an attenuation map into four classes (background, lungs, fat and soft tissue) on the basis of a 2-point Dixon MR sequence [20]. Although this technique disregards the potential influence of cortical bone, the authors reported that compared to other potential falsifying factors like repeated measurements and iodinated contrast medium, no significant deviation of the standardized uptake values (SUVs) were present except for the brain.

In PET/CT, sometimes from PET alone no definite statement concerning the nature of the PET-positive signal can be made (e.g. pulmonary nodule at the base of the lung vs hepatic metastasis). Thus, the low-dose CT needed for AC is also used in the diagnostic analysis of a PET/CT data set for anatomical correlation [23]. Although it does not replace a diagnostic CT, in many cases it grossly delineates neoplastic processes, especially in the bone, lungs and lymph nodes [24–26].

With the introduction of MR/PET systems, anatomical correlation over the whole coverage of PET will also be needed, similarly to low-dose CT. However, in contrast to low-dose CT just needing 20–30 s scan time for the whole body, dedicated MR sequences take considerably longer. Therefore, potential time constraints in MR/PET might not allow covering the whole body with fully diagnostic MR sequences in all instances. Morever, the AC for a recently introduced hybrid whole-body MR/PET system (Biograph mMR, Siemens Medical Solutions) works on the basis of the 2-point Dixon-based MR sequence investigated by Martinez-Möller et al. [20] and used in the current study.

Hence, the aim of our study was to evaluate whether this Dixon-based MR sequence can be used for the anatomical correlation and morphological delineation of PET-positive pathological processes and whether the SUVs of CT AC and MR AC data were significantly different. It has to be stressed at this point that merely its use compared to low-dose CT was investigated, not claiming that this sequence for AC can replace diagnostic MR.

Materials and methods

Patient population

In a prospective study 35 patients referred for the clinical staging and follow-up of known malignancy underwent a Dixon-based MR examination immediately after completion of the whole-body ^{18}F-fluorodeoxyglucose (FDG) PET/CT scan between February and June 2010. Approval of the Institutional Review Board was obtained. The malignant diseases for ^{18}F-FDG PET examinations comprised head and neck tumours (n=17), breast carcinomas (n=2), ovarian carcinoma (n=1), non-Hodgkin's lymphoma (n=5), malignant melanoma (n=3), oesophageal carcinoma (n=2), colon or gastric carcinomas (n=3), thyroid carcinoma (n=1) and cancer of unknown primary (n=1). The mean age of the 23 male and 12 female patients was 59.7 years (range 38–78 years).

PET/CT acquisition

All patients underwent a routine clinical ^{18}F-FDG protocol for oncological staging with a Siemens Biograph Sensation 64 PET/CT scanner (Siemens Medical Solutions, Erlangen, Germany). Patients fasted for at least 6 h before scanning, and blood glucose levels were measured just before injection to be below 150 mg/dl. Patients were injected with 350–500 MBq of ^{18}F-FDG depending on their weights and the acquisition was started after 90 min. For AC, low-dose CT (120 keV, 20 mAs) in the end-expiratory phase with oral (Telebrix 300 mg, Guerbet, Sulzbach, Germany) but not an intravenous contrast agent was performed. The acquisition was performed with the head pillow and knee

cushion, which were used on both modalities, in order to render positioning of the patient compatible in both scanners.

MR imaging

MR imaging was performed on a clinical 3T tomograph (Magnetom Verio, Siemens Medical Solutions, Erlangen, Germany) equipped with total imaging matrix technology, high-performance gradient systems (45 mT/m) and a slew rate of 200 T/m per s. Differences in patient positioning were reduced by the following measures: the patients were positioned in the MR scanner as similar as possible to the PET/CT (supine with arms up). Two six-element body matrix coils placed anteriorly were used in conjunction with two posterior spine clusters (three channels each) to optimize the signal to noise ratio (SNR). A coronal 2-point Dixon 3-D volumetric interpolated breath-hold examination (VIBE) T1-weighted (T1w) MR sequence was performed. Subsequently, the table was moved to the head/neck, thorax, abdomen and pelvis. In the thorax and abdomen the images were acquired in the end-expiratory phase similarly to low-dose CT. The parameters were as follows: integrated parallel acquisition technique factor 2, voxel size $4.1\times2.6\times2.6$ mm^3 (in-plane resolution × slice thickness), acquisition time 18 s, repetition time (TR)/echo time (TE) 3.6/1.225, matrix 79×192, number of excitations 1, field of view (FOV) 500 mm, phase FOV 72%, 1 slab with 128 slices, slice thickness 2.6 mm, flip angle 10°, bandwidth 960 kHz. To minimize artefacts from incomplete breath hold a centric k-space acquisition was chosen [27]. No contrast agent was administered for the MR studies. The software of the MR scanner automatically used the raw images to generate T1w in-/out-of-phase, water-only and fat-only images.

Data processing

Emission data were corrected for randoms, dead time, scatter and attenuation. An iterative reconstruction algorithm was applied [ordered subset expectation maximization (OSEM), four iterations and eight subsets, 5 mm full-width at half-maximum Gaussian smoothing, zoom 2.2]. Thereby, attenuation maps were obtained from the CT data by bilinear transformation in a conventional way implemented in the postprocessing software of the PET/CT scanner (PET_{AC_CT}) [13]. It is challenging to account for all non-rigid deformations between the MRI and CT images because of the acquisition in different scanners. Inaccuracies in the registration can have a severe impact on the SUV quantification [28]. To avoid influence from registration issues, MR-based attenuation maps were simulated by segmenting the CT data into four classes, as described previously [20]. Background was assigned an attenuation factor of 0 cm^{-1}, lung 0.018 cm^{-1}, fat 0.086 cm^{-1} and soft tissue 0.1 cm^{-1}. These attenuation maps were then used to reconstruct PET images with simulated MR-based AC (PET_{AC_MR}) normalizing them to have the same overall activity as in the PET_{AC_CT}.

Image analysis

Images were analysed by two experienced readers (one nuclear medicine physician and radiologist, one radiologist) blinded to the patient history. As a first step all the raw data of the four imaging sets (T1w in-/out-of-phase, fat-only, water-only) derived from the Dixon MR sequence, low-dose CT, PET_{AC_CT} and PET_{AC_MR} were transferred to a dedicated workstation (Syngo MMWP, Siemens Medical Solutions, Erlangen, Germany).

Then, PET_{AC_MR} were used to identify any region with focal uptake of ^{18}F-FDG. Next, T1w in-phase and PET_{AC_MR} data were loaded in the software (3D Fusion, Siemens Medical Solutions) that performs a rigid fusion automatically. In all cases the coregistration was evaluated and, if necessary, local adjustments were manually performed. For any detected focal uptake in PET_{AC_MR} the correct anatomical allocation was assigned in the fused data set (Fig. 1). All four imaging data sets (T1w in-/out-of-phase, fat-only, water-only) were evaluated for the presence of a distinct lesion corresponding with the focal uptake. Subsequently, the same procedure was performed with the PET_{AC_CT}: hereby, for any focal uptake in the PET_{AC_CT} the low-dose CT was used for anatomical correlation and for identification of a potential lesion.

The certainty of the anatomical correlation and the presence of a possible morphological lesion (further named $Scoring_{CT}$ and $Scoring_{MR}$, respectively) was assessed separately for Dixon-based MR and low-dose CT by using a 4-point scale: 0: no anatomical correlation possible/no morphological correlate detectable, 1: uncertain anatomical correlation/no morphological correlate detectable, 2: good anatomical correlation/questionable morphological correlate and 3: excellent anatomical correlation with a clear morphological correlate.

Finally, for comparison of the quantification capability between the low-dose CT and the simulated Dixon-based PET AC the SUV_{mean} (SUV_{AC_CT} and SUV_{AC_MR}) was measured for all positive lesions. Thereby, both the PET_{AC_CT} and PET_{AC_MR} were simultaneously loaded in the commercially available TrueD application at the postprocessing workstation. The SUV_{mean} was measured by using a 50% isocontour region of interest (ROI) which was placed over the lesion in the PET_{AC_CT} and copied to the PET_{AC_MR}. In the case of multiple PET-positive lesions only up to five lesions per organ system were chosen to avoid bias from single patients. In addition the modality which outlined the lesions at its best was used for size measurements (e.g. CT for a pulmonary nodule).

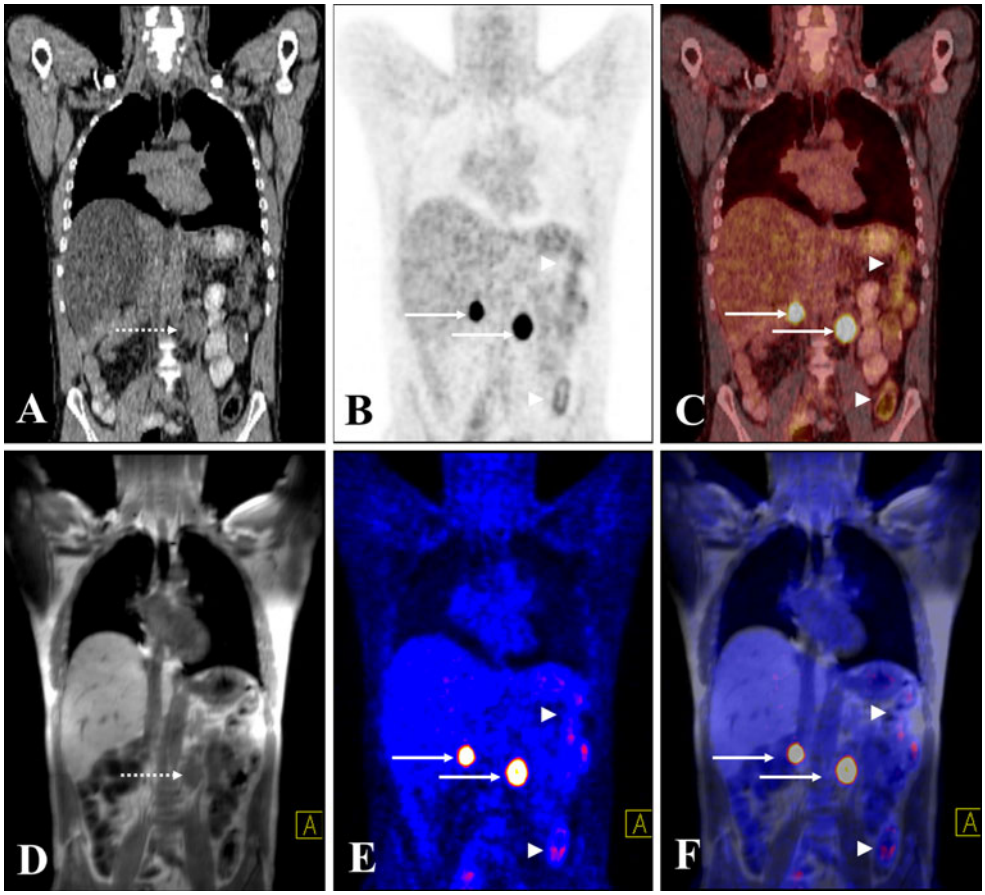

Fig. 1 Set of images in a 47-year-old patient with retroperitoneal lymph node metastases from colon cancer. Coronal reformatted low-dose CT (**a**) and Dixon T1w (**d**) images demonstrate a higher soft tissue contrast for MR (e.g. liver) and higher spatial resolution for CT (e.g. delineation of ribs). Both PET_{AC_CT} (**b**) and PET_{AC_MR} (**e**) show two focal areas with increased ^{18}F-FDG uptake in the abdomen (*arrows*, *continuous line*). Only for the large lesion a morphological correlate could be found both in low-dose CT and Dixon-based T1w (*arrows*, *dashed line* in **a** and **d**). Image fusion for PET/CT (**c**) and MR/PET (**f**) demonstrates the anatomical location of the PET-positive lesions in the retroperitoneum (*arrows*, *continuous line*). A faint to moderate tubular uptake in the left abdomen (*arrowheads* in **b** and **e**) is projected on the descending colon in the fused images (*arrowheads* in **c** and **f**) and represents physiological bowel activity

Statistical analysis

Statistical analysis was performed using MedCalc 6.15 software package for Windows. A p value less than 0.05 was considered statistically significant. The Kolmogorov-Smirnov test was used to test for normal distribution. For calculating the overall statistical differences between mean values, a nonparametric Wilcoxon matched-pairs signed rank test was used. Linear regression analysis was used for correlation between SUV_{AC_CT} and SUV_{AC_MR} and $Scoring_{CT}$ and $Scoring_{MR}$.

Results

Overall, in the 35 patients included in the study both PET_{AC_MR} and PET_{AC_MR} identified 81 lesions with increased focal uptake. In total, 10 bone metastases, 5 liver metastases, 8 lung nodules, 13 primary head/neck malignancies, 38 lymph node metastases and 7 soft tissue lesions were present. For details see Table 1.

Anatomical correlation of PET-positive lesions

No significant difference was found for scoring the correlation of PET-positive lesions with anatomical structures on low-dose CT and the Dixon-based MR data sets (mean $Scoring_{CT}$ 2.51±0.85 and $Scoring_{MR}$ 2.37±0.87, respectively; p=0.1909). The results for the different organ systems are presented in Table 2. Linear regression analysis found a highly significant, but low to moderate correlation coefficient between $Scoring_{CT}$ and $Scoring_{MR}$ (correlation coefficient r=0.5678, 95% confidence interval 0.3989–0.6994, p<0.0001). This shows that in a substantial number of lesions the rating was discrepant.

In detail, low-dose CT performed better in six cervical, three thoracic and three abdominal lymph nodes. This was

Table 1 Patient characteristics

Patient	Age	Malignancy	PET-positive findings (*n*)	Patient	Age	Malignancy	PET-positive findings (*n*)
1	48	Caecum Ca.	Liver metastases (2)	19	50	Mandibular Ca.	–
2	59	Non-Hodgkin's lymphoma	Retroperitoneal lymph node bulks (2)	20	61	CUP	Bone metastases (5)
3	61	Oropharyngeal Ca.	Primary tumour	21	54	Oropharyngeal Ca.	Primary tumour
			Lymph node metastasis (1)				Lymph node metastases (2)
4	65	Oropharyngeal Ca.	Lymph node metastasis (1)	22	71	Non-Hodgkin's lymphoma	Infracarinal lymph node (1)
5	48	Sigmoid Ca.	Liver metastases (3)	23	66	Malignant melanoma	Soft tissue metastases (2)
			Unclear intra-abdominal uptake (lymph node vs colon)				Lung metastases (2)
							Lymph node metastasis (1)
6	47	Hypopharyngeal Ca.	Lymph node metastases (2)	24	76	Malignant melanoma	Postoperative scar tissue right axilla shoulder tendinopathy (high activity)
			Lung metastasis (1)				
7	59	Oesophageal Ca.	Primary tumour	25	38	Oropharyngeal Ca.	Primary tumour
8	68	Oropharyngeal Ca.	Primary tumour	26	54	Hypopharyngeal	Primary tumour
			Lymph node metastases (4)				Lymph node metastases (3)
9	67	Breast Ca.	Lung metastasis (1)	27	57	Breast Ca.	Lymph node metastases (3)
			Lymph node metastases (2)				Bone metastases (2
			Bone metastases (2)				Lung metastases (2)
10	77	Ovarian Ca.	–	28	61	Oropharyngeal Ca.	Primary tumour
11	65	Non-Hodgkin's lymphoma	Lymph node (1)	29	53	Oropharyngeal Ca.	Primary tumour
							Lymph node metastases (3)
12	70	Oropharyngeal Ca.	Primary tumour	30	46	Oesophageal Ca.	Primary tumour
			Two lymph node metastases				Lymph node metastases (3)
13	61	Oropharyngeal Ca.	Primary tumour	31	44	Oropharyngeal Ca.	Primary tumour
			Lymph node metastases (2)				
14	71	Non-Hodgkin's lymphoma	–	32	47	Colonic Ca.	Lymph node metastases (2)
15	47	Parotid Ca.	–	33	67	Oropharyngeal Ca.	Primary tumour
16	60	Malignant melanoma	Bone metastasis (1)	34	78	Follicular thyroid Ca.	Lung metastases (2)
17	49	Oropharyngeal Ca.	Primary tumour	35	71	Oropharyngeal Ca.	Primary tumour
			Lymph node metastasis (1)				Lymph node metastases (2)
18	73	Non-Hodgkin's lymphoma	–				

Ca. cancer, *CUP* cancer of unknown primary

Table 2 Quality of anatomical correlation and delineation of PET-positive findings in low-dose CT and Dixon-based MR sequences

Lesion type		No.	Mean size in mm ± SD (range)	SUV_{AC_CT} mean ± SD (range)	SUV_{AC_MR} mean ± SD (range)	$Scoring_{CT}$	$Scoring_{MR}$	No. of positive correlates in low-dose CT	No. of positive correlates in MR: in/out/fat/water
Lymph node metastases	All	38	13.0±7.4 (6–40)	6.52±4.21 (1. 20–22.39)	6.48±4.33 (1.18–23.06)	2.79±0.53	2.37±0.88	36	30/23/23/24
	Neck	24	15.0±7.7 (6–40)	7.09±4.54 (1.47–22.39)	7.14±4.66 (1.54–23.06)	2.83±0.48	2.58±0.71	23	20/13/15/16
	Thorax	7	13.7±4.8 (8–22)	4.13±1.54 (1.20–5.56)	4.06±1.54 (1.18–5.85)	2.86±0.38	2.29±0.76	7	6/6/4/4
	Abdominal	7	16.3±9.1 (8–30)	6.97±4.45 (2.73–14.96)	7.22±4.59 (2.89–15.32)	2.57±0.79	1.71±1.25	6	4/4/4/3
Lung metastases		8	10.1±1.7 (8–12)	3.46±1.53 (2.02–6.08)	3.30±1.47 (1.97–5.79)	3[a]	2.75±0.46	8	7/7/5/7
Bone metastases		10	20.6±7.0 (12–32)	3.33±1.16 (1.91–5.03)	3.10±1.13 (1.47–4.92)	3[a]	2.70±0.48	10	9/3/8/5
Liver metastases		5	35.2±10.9 (25–52)	5.66±1.58 (4.25–7.48)	5.90±1.85 (4.38–8.06)	1.80±1.10	3[a]	2	4/2/3/2
Pharyngeal tumour		13	[b]	10.07±6.56 (2.77–27.55)	9.80±6.58 (2.91–27.50)	1.77±0.93	2.08±0.86	6	7/6/5/6
Other soft tissue pathologies[c]		7	[b]	6.73±2.74 (2.71–9.88)	6.70±2.65 (3.14–10.41)	1.57±1.27	1.57±1.27	5	4/3/2/3
Total		81	–	6.36±4.47 (1.20–27.55)	6.31±4.52 (1.18–27.50)	2.51±0.85	2.37±0.87	66	61/44/46/45

[a] Same results for all lesions, SD=0

[b] Not analysable on low-dose and/or Dixon MR

[c] Muscle metastases, oesophageal cancer, postoperative scar tissue, tendinopathy

mainly due to the better anatomical resolution of CT compared to the MR sequence used as the mean size of these lymph nodes was 7.5 mm in contrast to 13.0 mm for all lymph nodes. Two lung nodules and three rib metastases could be better depicted on CT (Fig. 2). One small metastasis (8 mm) from malignant melanoma in the abdominal wall was better delineated in CT due to surrounding subcutaneous fat. In contrast, Dixon-based MR was able to demonstrate the primary tumour of four head/neck patients, one cervical lymph node metastasis and one postoperative axillary soft tissue scar better than low-dose CT. Moreover, three of the five liver metastases could be only detected on MR (Fig. 3). However, the remaining two liver lesions were so large and centrally necrotic that even low-dose CT with its low soft tissue contrast was able show them.

Concerning the analysis of the different images (T1w in-/out-of-phase, water-only, fat-only) derived from the Dixon sequence the data presented in Table 2 indicate that especially for lymph node metastases the T1w in phase images provided the highest number of anatomical correlates for PET-positive lesions. For bone metastases T1w in-phase and fat-only images were best suited for lesion detection. In all other PET-positive lesions no single image set showed a clear tendency to considerably better results compared to the others.

Only in one patient (5 in Table 1) a potentially false-positive finding occurred as high uptake in the abdomen could not correctly be assigned to bowel activity or a potential lymph node metastasis in sigmoid cancer. However, also low-dose CT was not able to solve this issue. Good anatomical coregistration could be found in the case of physiological uptake, e.g. in the bowel, brown fat or in the case of ureteral retention. Several incidental findings (e.g. pleural effusion, chronic sinusitis) could both be detected on low-dose CT and Dixon-based MR. Coregistration between PET_{AC_MR} and the Dixon-based MR sequence proved valuable for PET-positive lesions and helped in the diagnostic assessment of physiological tracer uptake of bowel or brown fat.

Correlation between SUV_{AC_CT} and SUV_{AC_MR}

No statistical difference could be found between the SUV_{AC_CT} and SUV_{AC_MR} (p=0.1919, Table 2). Moreover, a high linear correlation coefficient in the SUVs for the PET images reconstructed by attenuation maps from low-dose CT or simulated MR-based attenuation was found (correlation coefficient r=0.9975, 95% confidence interval 0.9961–0.9948, p<0.0001, Fig. 4). Consequently, examination of the PET images revealed no differences in the clinical interpretations of the PET scans for all of the patients. Neither false-positive nor false-negative findings in PET_{AC_MR} relative to the findings in PET_{AC_CT} were observed. In our work, the bone metastases showed the largest mean difference with a decrease of 7.46% on average of SUV_{AC_MR} compared to SUV_{AC_CT}.

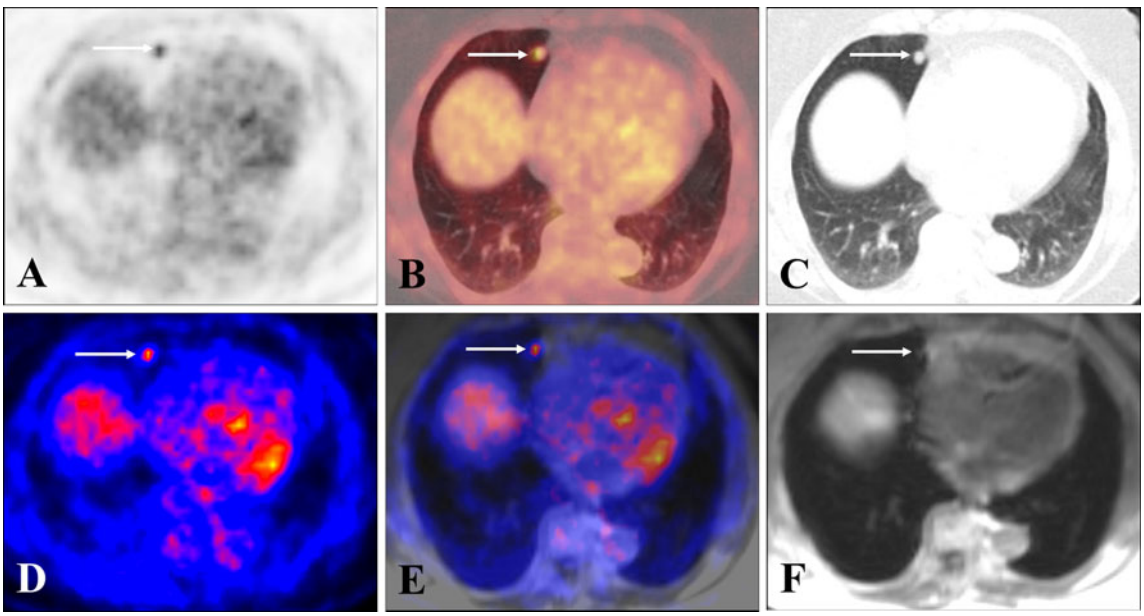

Fig. 2 Images from a 78-year-old woman with follicular thyroid cancer and lung metastases. Both PET_{AC_CT} (**a**), PET_{AC_MR} (**d**) and image fusion with low-dose CT (**b**) and Dixon T1w (**e**) show a focal high uptake in the cardiophrenic angle on the right side. **c** and **f** illustrate that low-dose CT (**c**) in the lung window is clearly superior to Dixon T1w (**f**) in the morphological delineation of the lung nodule which appears very blurry in MR

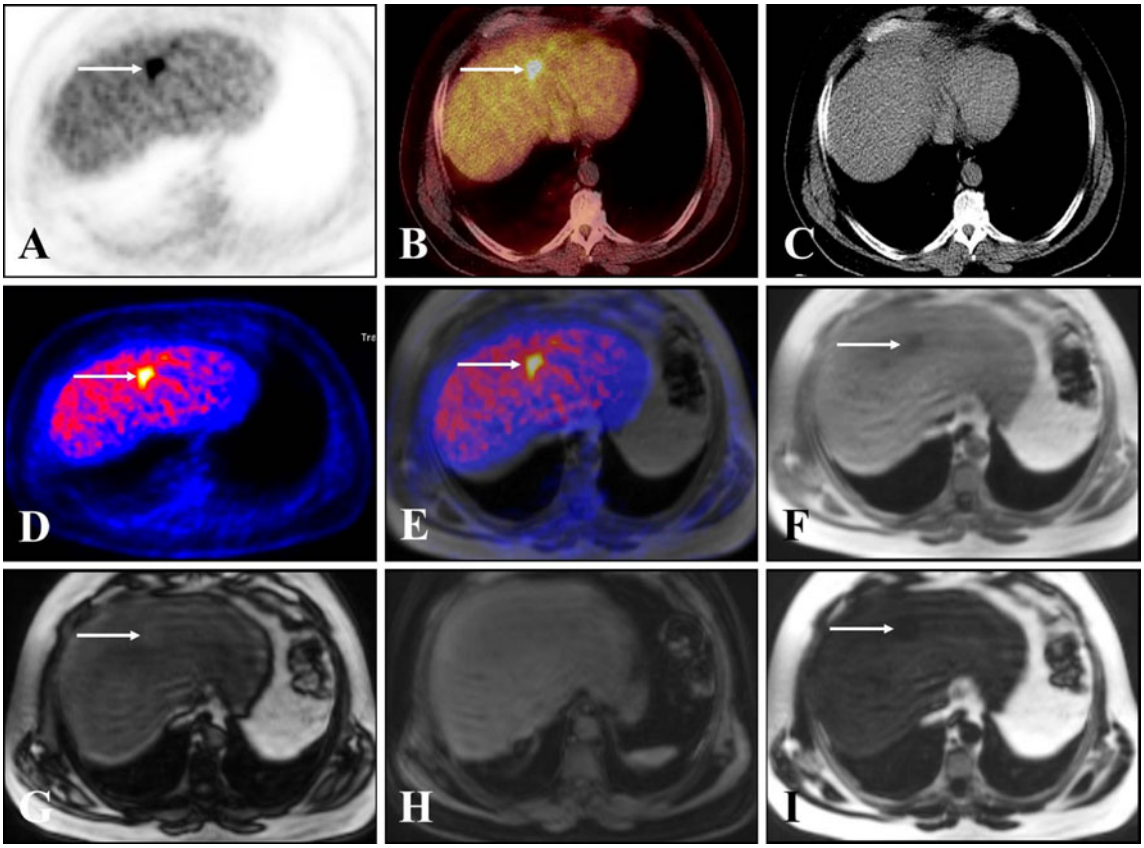

Fig. 3 Set of images in a 48-year-old patient with a liver metastasis from sigmoid cancer. High liver uptake is found both in PET_{AC_CT} (**a**) and PET_{AC_MR} (**d**), whereas image fusion with low-dose CT (**b**) and Dixon T1w (**e**) allow for better anatomical correlation. In low-dose CT due to its low soft tissue contrast no anatomical correlate for the liver metastasis could be found (**c**). **f**–**i** present the different sets created from the raw data of the Dixon sequence (**f**: T1w in-phase, **g**: T1w out-of-phase, **h**: water-only and **i**: fat-only). The complementary value of different reconstructions can be appreciated as the liver metastases are outlined with different quality in T1w in-phase (**f**), T1w out-of-phase (**g**) and fat-only (**i**). No correlate can be found in the water-only image (**h**)

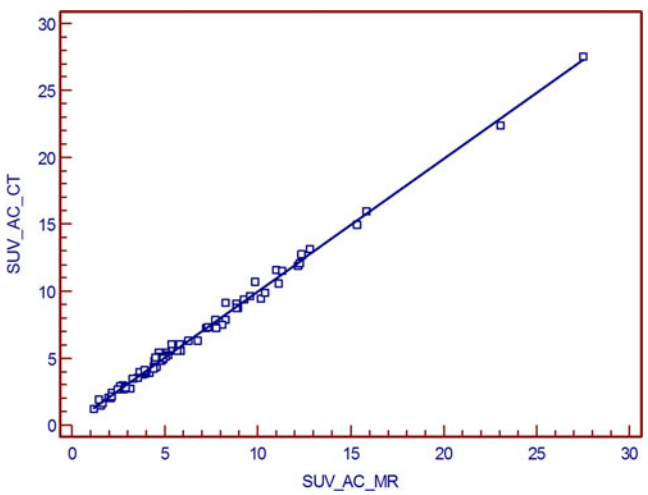

Fig. 4 Correlation of SUV_{AC_CT} and SUC_{AC_MR} based on the SUV_{mean} show a high linear correlation with nearly complete agreement (r=0.9975, 95% confidence interval 0.9961–0.9948, p<0.0001)

Discussion

In this study we showed that the Dixon MR sequence implemented in a recently introduced integrated MR/PET system is promising for identification of PET-positive lesions. We found no statistical difference in lesion detection compared to low-dose CT used in PET/CT, with specific advantages in different body areas for each modality. Finally, no significant difference in SUVs between the MR- and CT-based attenuation-corrected PET was found.

The advent of whole-body MR/PET raises the necessity for new approaches in AC as the information on radio-density as provided by CT is not offered by MR imaging. The data we presented have shown that the method described by Martinez-Möller et al. using Dixon MR sequences for AC [20] provides a similar capability of anatomical coregistration as compared to low-dose CT. Besides dedicated MR sequences for imaging specific organs systems in an MR/PET system (e.g. liver in patients with colorectal cancer) due to time constraints not every

patient might undergo diagnostic MR sequences for the whole body. Due to technical issues, the AC sequence will be used anyway in the foreseeable future for AC in the recently introduced hybrid MR/PET (Biograph mMR, Siemens Medical Solutions). It has to be stressed at this point that the aim of our study was to compare the techniques used for AC in MR/PET and PET/CT. We do not claim that the Dixon MR sequence can replace diagnostic MR sequences or is of equal diagnostic performance as a contrast-enhanced CT. Nevertheless, the possibility of reusing the images acquired for AC also for anatomical correlation could be an attractive scenario. This might reduce examination times and improve both patient comfort and cost-effectiveness.

In the recent hybrid MR/PET system this sequence is acquired with the start of the PET acquisition. It takes ~18 s during one breath hold per bed position, but consequentially shows a considerably lower spatial resolution (4.1×2.6×2.6 mm^3, 94×256 matrix) compared to low-dose CT reconstructed with a 512×512 matrix and a soft tissue kernel [29]. However, in our study the improved soft tissue contrast provided by MR and the possibility of creating different image sets (T1w in-/out-of-phase, water-only and fat-only contrast) resulted in no significant differences for functional-morphological correlation between the two modalities. In addition, this nearly isotropic 3-D sequence allows easy multiplanar reformation which also might help when a non-isotropic diagnostic MR sequence acquired in a specific plane does not describe the anatomical position of pathology exactly. However, as definite protocols for whole-body MR/PET examinations are to be worked out in the future this hypothesis has to be proven in further studies.

The high expectations put on an integrated whole-body MR/PET are mainly driven by the advantage MR offers in detecting hepatic lesions, head/neck and intracranial abnormalities [4, 7, 8, 30, 31]. The limited number of different types of lesions analysed in this study do not allow for statistical analysis of organ-specific pathologies. However, compared to low-dose CT the data presented for the Dixon-based MR sequence show a trend to a better performance for hepatic and head/neck pathologies (Table 2). This primarily is the effect of a higher soft tissue contrast in these regions. For bone metastases as in conventional diagnostic MR our data indicate that T1w in-phase and fat-only images from the Dixon sequence showing the replacement of fat containing bone marrow by neoplastic cells are best suited [32]. As reported in the literature and also in our study the T1w in-phase images scored best for lymph node metastases [33, 34].

CT tended to perform better for lymph node metastases, especially when they were small and located at anatomically difficult areas (e.g. thoracic, abdominal). CT outlines them more easily due to the surrounding fat and the higher spatial resolution. Three lesions in the ribs were better outlined in low-dose CT as MR is reported to suffer from

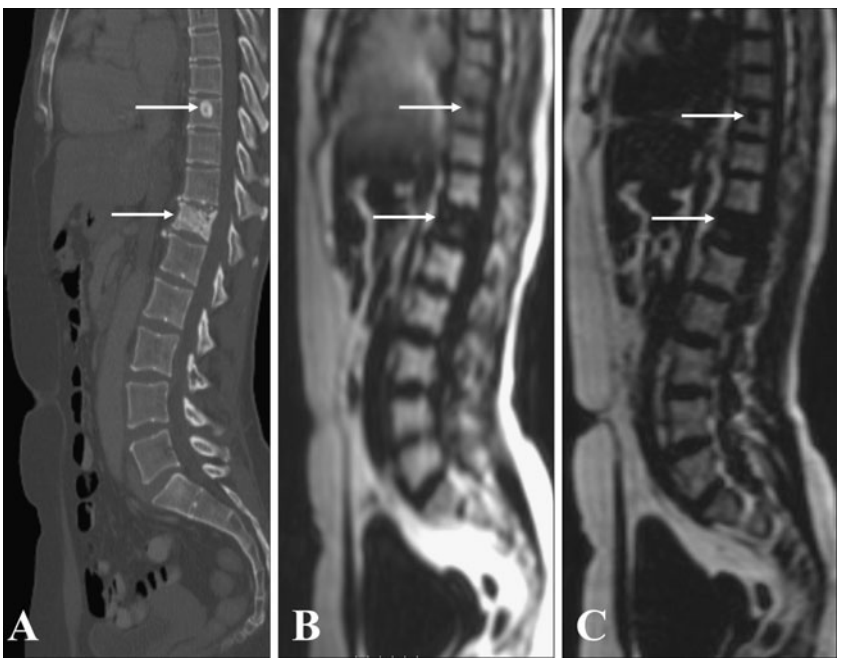

Fig. 5 Sagittal reformatted of low-dose CT demonstrates the high spatial resolution in a patient with two bone metastases (**a**). Inferior spatial resolution resulting in a blurry impression can be found in the fat-only image of the Dixon MR used in the study (**b**). Preliminary efforts to modify the sequence for a higher resolution result in a better delineation of anatomical details (**c**). However, the spatial resolution of this sequence is still inferior to that of a low-dose CT

limitation in this anatomically difficult region [35]. For lung nodules the inferior spatial resolution both for whole-body and dedicated, lung-specific MR sequences compared to CT is known to result in a lower sensitivity [4, 10, 36, 37]. In the small number of lung nodules in our study, CT tended to perform only slightly better. However, it has to be stated that identifying a lung nodule in MR in a region with known positive PET signal as in our study is much easier than a prospective detection. In this context, image fusion in our study proved to be helpful even if we did not analyse its contribution in detail.

A potential improvement of these limitations might be the use of a higher resolution Dixon MR sequence at the expense of an increased imaging time. But as conventional PET scanners measure 2–3 min per bed position [23] such an extension towards a respiratory-triggered Dixon image with higher resolution appears feasible. We tentatively evaluated this hypothesis in a small number of patients by applying a Dixon-based MR sequence with higher resolution in several anatomical locations. The sequence was modified by reducing the coverage in z direction by almost 50%, thus keeping the acquisition time of 18 s [matrix 94×256, voxel size 2.0×1.8×2.6 mm^3 (in-plane resolution × slice thickness), FOV 450 mm, phase FOV 41%, 1 slab with 122 slices]. This resulted for the same total coverage in approximately twice the number of breath holds and imaging time for a whole-body examination but showed considerably higher anatomical details (Fig. 5).

As a corollary result, our data confirmed the results by Martinez-Möller et al. [20] that the reconstruction by use of a segmented attenuation map with four tissue classes has no significant impact on SUVs and thus on the clinical interpretation of the images for all patients. The small differences between PET_{AC_CT} and PET_{AC_MR} might be explained due to neglecting possible inhomogeneities within the four different tissue classes in MR as opposed to radiodensity in CT. This corroborates the results of the former study in another patient collective with different types of lesions.

Our study has several limitations: firstly, we did not provide a gold standard based on histopathology or follow-up imaging for the lesions detected on PET. However, the aim of our study was to investigate the anatomical correlation between low-dose CT and Dixon MR and not to provide a specific diagnosis. Secondly, as in the study by Martinez-Möller et al. [20], the PET_{AC_MR} was reconstructed by attenuation maps from simulated MR-based segmentation without using the MR data set itself, in order to avoid errors resulting from inaccurate registration [28, 38].

Finally, besides a global investigation the individual numbers of organ-specific lesions were not high enough for statistical analyses comparing low-dose CT and Dixon MR. Thus, for single lesions (e.g. bone metastases, lung nodules) just a tendency could be shown whether MR is superior to CT or vice versa. However, the aim of our study was to show the feasibility for anatomical correlation of a Dixon MR sequence which is automatically acquired with the start of PET in a recently introduced hybrid MR/PET scanner for AC. Thus, larger and prospective studies on hybrid MR/PET systems are now warranted.

Conclusion

A Dixon MR imaging sequence can be used for anatomical correlation of PET-positive lesions besides its use for AC. As no significant difference could be found between the two techniques, a Dixon MR therefore could replace the function of a low-dose CT in an MR/PET scanner in many instances. This minimizes the need for additional sequences in areas of the body not necessarily covered by fully diagnostic MR sequences and thus helps to overcome possible time constraints.

Acknowledgments We thank Brigitte Dzewas and Sylvia Schachoff and the whole PET team for their excellent technical assistance.

Conflicts of interest None.

References

1. Antoch G, Bockisch A. Combined PET/MRI: a new dimension in whole-body oncology imaging? Eur J Nucl Med Mol Imaging 2009;36:S113–20.
2. Zaidi H, Mawlawi O, Orton CG. Point/counterpoint. Simultaneous PET/MR will replace PET/CT as the molecular multimodality imaging platform of choice. Med Phys 2007;34:1525–8.
3. Seemann MD. Whole-body PET/MRI: the future in oncological imaging. Technol Cancer Res Treat 2005;4:577–82.
4. Antoch G, Vogt FM, Freudenberg LS, Nazaradeh F, Goehde SC, Barkhausen J, et al. Whole-body dual-modality PET/CT and whole-body MRI for tumor staging in oncology. JAMA 2003;290:3199–206.
5. Fonti R, Salvatore B, Quarantelli M, Sirignano C, Segreto S, Petruzziello F, et al. 18F-FDG PET/CT, 99mTc-MIBI, and MRI in evaluation of patients with multiple myeloma. J Nucl Med 2008;49:195–200.
6. Angtuaco EJC, Fassas ABT, Walker R, Sethi R, Barlogie B. Multiple myeloma: clinical review and diagnostic imaging. Radiology 2004;231:11–23.
7. Herholz K, Coope D, Jackson A. Metabolic and molecular imaging in neuro-oncology. Lancet Neurol 2007;6:711–24.
8. Ruf J, Lopez Hänninen E, Böhmig M, Koch I, Denecke T, Plotkin M, et al. Impact of FDG-PET/MRI image fusion on the detection of pancreatic cancer. Pancreatology 2006;6:512–9.
9. Schmidt GP, Haug AR, Schoenberg SO, Reiser MF. Whole-body MRI and PET-CT in the management of cancer patients. Eur Radiol 2006;16:1216–25.
10. Lauenstein TC, Goehde SC, Herborn CU, Goyen M, Oberhoff C, Debatin JF, et al. Whole-body MR imaging: evaluation of patients for metastases. Radiology 2004;233:139–48.
11. Beer AJ, Eiber M, Souvatzoglou M, Schwaiger M, Krause BJ. Radionuclide and hybrid imaging of recurrent prostate cancer. Lancet Oncol 2011;12:181–91.

12. Beer AJ, Eiber M, Souvatzoglou M, Holzapfel K, Ganter C, Weirich G, et al. Restricted water diffusibility as measured by diffusion-weighted MR imaging and choline uptake in (11)C-choline PET/CT are correlated in pelvic lymph nodes in patients with prostate cancer. Mol Imaging Biol 2011;13:352–61.
13. Kinahan PE, Hasegawa BH, Beyer T. X-ray-based attenuation correction for positron emission tomography/computed tomography scanners. Semin Nucl Med 2003;33:166–79.
14. Zaidi H. Is MR-guided attenuation correction a viable option for dual-modality PET/MR imaging? Radiology 2007;244:639–42.
15. Catana A, Van Der Kouwe A, Benner T, Hamm M, Michel C, Fischl B, et al. Is accurate bone segmentation required for MR-based PET attenuation correction? Proc Int Soc Magn Reson Med 2009:593.
16. Delso G, Martinez-Möller A, Bundschuh RA, Ladebeck R, Candidus Y, Faul D, et al. Evaluation of the attenuation properties of MR equipment for its use in a whole-body PET/MR scanner. Phys Med Biol 2010;55:4361–74.
17. Keereman V, De Deene Y, Lemahieu I, Vandenberghe S. Estimation of attenuation maps from UTE derived R2 image. Proc Int Soc Magn Reson Med 2009:2774.
18. Hofmann M, Steinke F, Scheel V, Charpiat G, Farquhar J, Aschoff P, et al. MRI-based attenuation correction for PET/MRI: a novel approach combining pattern recognition and atlas registration. J Nucl Med 2008;49:1875–83.
19. Zaidi H, Montandon M, Slosman DO. Magnetic resonance imaging-guided attenuation and scatter corrections in three-dimensional brain positron emission tomography. Med Phys 2003;30:937–48.
20. Martinez-Möller A, Souvatzoglou M, Delso G, Bundschuh RA, Chefd'hotel C, Ziegler SI, et al. Tissue classification as a potential approach for attenuation correction in whole-body PET/MRI: evaluation with PET/CT data. J Nucl Med 2009;50:520–6.
21. Schulz V, Torres-Espallardo I, Renisch S, Hu Z, Ojha N, Börnert P, et al. Automatic, three-segment, MR-based attenuation correction for whole-body PET/MR data. Eur J Nucl Med Mol Imaging 2011;38:138–52. doi:10.1007/s00259-010-1603-1.
22. Steinberg J, Jia G, Sammet S, Zhang J, Hall N, Knopp MV. Three-region MRI-based whole-body attenuation correction for automated PET reconstruction. Nucl Med Biol 2010;37:227–35.
23. Boellaard R, O'Doherty MJ, Weber WA, Mottaghy FM, Lonsdale MN, Stroobants SG, et al. FDG PET and PET/CT: EANM procedure guidelines for tumour PET imaging: version 1.0. Eur J Nucl Med Mol Imaging 2010;37:181–200.
24. Elstrom RL, Leonard JP, Coleman M, Brown RKJ. Combined PET and low-dose, noncontrast CT scanning obviates the need for additional diagnostic contrast-enhanced CT scans in patients undergoing staging or restaging for lymphoma. Ann Oncol 2008;19:1770–3.
25. Pfannenberg AC, Aschoff P, Brechtel K, Müller M, Klein M, Bares R, et al. Value of contrast-enhanced multiphase CT in combined PET/CT protocols for oncological imaging. Br J Radiol 2007;80:437–45.
26. Schaefer NG, Hany TF, Taverna C, Seifert B, Stumpe KDM, von Schulthess GK, et al. Non-Hodgkin lymphoma and Hodgkin disease: coregistered FDG PET and CT at staging and restaging–do we need contrast-enhanced CT? Radiology 2004;232:823–9.
27. Maki JH, Chenevert TL, Prince MR. The effects of incomplete breath-holding on 3D MR image quality. J Magn Reson Imaging 1997;7:1132–9.
28. Beyer T, Weigert M, Quick HH, Pietrzyk U, Vogt F, Palm C, et al. MR-based attenuation correction for torso-PET/MR imaging: pitfalls in mapping MR to CT data. Eur J Nucl Med Mol Imaging 2008;35:1142–6.
29. Horger M, Claussen CD, Bross-Bach U, Vonthein R, Trabold T, Heuschmid M, et al. Whole-body low-dose multidetector row-CT in the diagnosis of multiple myeloma: an alternative to conventional radiography. Eur J Radiol 2005;54:289–97.
30. Lauenstein TC, Semelka RC. Emerging techniques: whole-body screening and staging with MRI. J Magn Reson Imaging 2006;24:489–98.
31. Ng S, Yen T, Chang JT, Chan S, Ko S, Wang H, et al. Prospective study of [18F]fluorodeoxyglucose positron emission tomography and computed tomography and magnetic resonance imaging in oral cavity squamous cell carcinoma with palpably negative neck. J Clin Oncol 2006;24:4371–6.
32. Vanel D, Bittoun J, Tardivon A. MRI of bone metastases. Eur Radiol 1998;8:1345–51.
33. van den Brekel MW. Lymph node metastases: CT and MRI. Eur J Radiol 2000;33:230–8.
34. Castelijns JA, van den Brekel MWM. Imaging of lymphadenopathy in the neck. Eur Radiol 2002;12:727–38.
35. Venkitaraman R, Cook GJR, Dearnaley DP, Parker CC, Khoo V, Eeles R, et al. Whole-body magnetic resonance imaging in the detection of skeletal metastases in patients with prostate cancer. J Med Imaging Radiat Oncol 2009;53:241–7.
36. Bruegel M, Gaa J, Woertler K, Ganter C, Waldt S, Hillerer C, et al. MRI of the lung: value of different turbo spin-echo, single-shot turbo spin-echo, and 3D gradient-echo pulse sequences for the detection of pulmonary metastases. J Magn Reson Imaging 2007;25:73–81.
37. Vogt FM, Herborn CU, Hunold P, Lauenstein TC, Schröder T, Debatin JF, et al. HASTE MRI versus chest radiography in the detection of pulmonary nodules: comparison with MDCT. AJR Am J Roentgenol 2004;183:71–8.
38. Martinez-Möller A, Souvatzoglou M, Navab N, Schwaiger M, Nekolla SG. Artifacts from misaligned CT in cardiac perfusion PET/CT studies: frequency, effects, and potential solutions. J Nucl Med 2007;48:188–93.